

Hybrid Quantum-Classical Photonic Neural Networks

Tristan Austin,* Andrew Hayman, and Nir Rotenberg
*Centre for Nanophotonics, Department of Physics,
Engineering Physics, and Astronomy, Queen's University.*

Simon Bilodeau
Department of Electrical Engineering, Princeton University

Bhavin J. Shastri†
*Centre for Nanophotonics, Department of Physics,
Engineering Physics, and Astronomy, Queen's University. and
Smith Engineering, Department of Electrical Engineering, Queen's University*

Neuromorphic (brain-inspired) photonics leverages photonic chips to accelerate artificial intelligence [1], offering high-speed and energy efficient solutions for use in RF communication [2], tensor processing [3], and data classification [4, 5]. However, the limited physical size of integrated photonic hardware constrains network complexity and computational capacity. In light of recent advances in photonic quantum technology [6], it is natural to utilize quantum exponential speedup to scale photonic neural network capabilities. Here we show a combination of classical network layers with trainable continuous variable quantum circuits yields hybrid networks with improved trainability and accuracy. On a classification task, hybrid networks achieve the same performance when benchmarked against fully classical networks that are twice the size. When the bit precision of the optimized networks is reduced through added noise, the hybrid networks still achieve greater accuracy when evaluated at state of the art bit precision. These hybrid quantum classical networks demonstrate a unique route to improve computational capacity of integrated photonic neural networks without increasing the network size.

I. INTRODUCTION

Neuromorphic photonics is a promising accelerator for artificial intelligence and brain-inspired computing [1], capable of quickly diagonalizing matrices [7], separating mixed RF signals [2], and classifying spoken vowels and handwritten digits [5, 8]. Neuromorphic networks consist of layers of interconnected neurons, as sketched in Fig. 1, and, like the brain, the complexity of these networks is largely determined by the number of connections between these neurons. On neuromorphic photonic platforms, such as silicon [9], silicon nitride [10], and lithium niobate [11], these neurons are implemented by circuitry comprised of photonic resonators, waveguides, modulators, and detectors [12, 13], resulting in high bandwidth, low loss, and ultralow latency networks [1, 14]. Yet the relatively large size of these optical components, particularly in comparison with their electronic counterparts, limits the size of neuromorphic photonic networks and hence their complexity and power.

Here, we explore a new route to increasing the network complexity, namely by replacing layers of classical neurons with a quantum neural network. More specifically, we envision using a continuous variable (CV) photonic network [15–17], of the kind in which quantum advantage was recently demonstrated [6, 18], which is built on the

same platforms, using the same devices, as typical neuromorphic photonic devices. Using an exemplary classification task, we show that such hybrid quantum-classical neuromorphic networks can outperform fully classical networks both in terms of ease of training and overall accuracy. This advantage is more significant for smaller networks with $\lesssim 350$ weights (for reference, a state-of-the-art 3-layer $6 \times 6 \times 6 \times 6$ integrated photonic network has 98 weights [19]). Finally, we show that within this range, hybrid neuromorphic networks are sufficiently robust to noise, reinforcing that hybrid quantum-classical photonics may play an important role in unlocking the full potential of brain-inspired hardware.

II. HYBRID CONTINUOUS VARIABLE NEURAL NETWORKS

We begin by constructing models of both hybrid and fully classical neural networks, as sketched out in Fig. 1a and b, respectively. The difference between the two is that the hidden layer of the classical network (shaded region of Fig. 1b) is replaced by a CV quantum neural network (CVQNN) [15] as shown by the shaded region of the hybrid network (Fig. 1a). Both cases have identical input ($W^{(i)}$) and output ($W^{(o)}$) layers, typically fully-connected classical feed-forward networks, whose dimensions depend on the task to be performed. Here, we select a classification task because, while challenging, it is well-suited for feed-forward neural networks. More specifically, we synthetically generate 1000 samples [22] (700

* 17tna@queensu.ca

† shastri@ieee.org

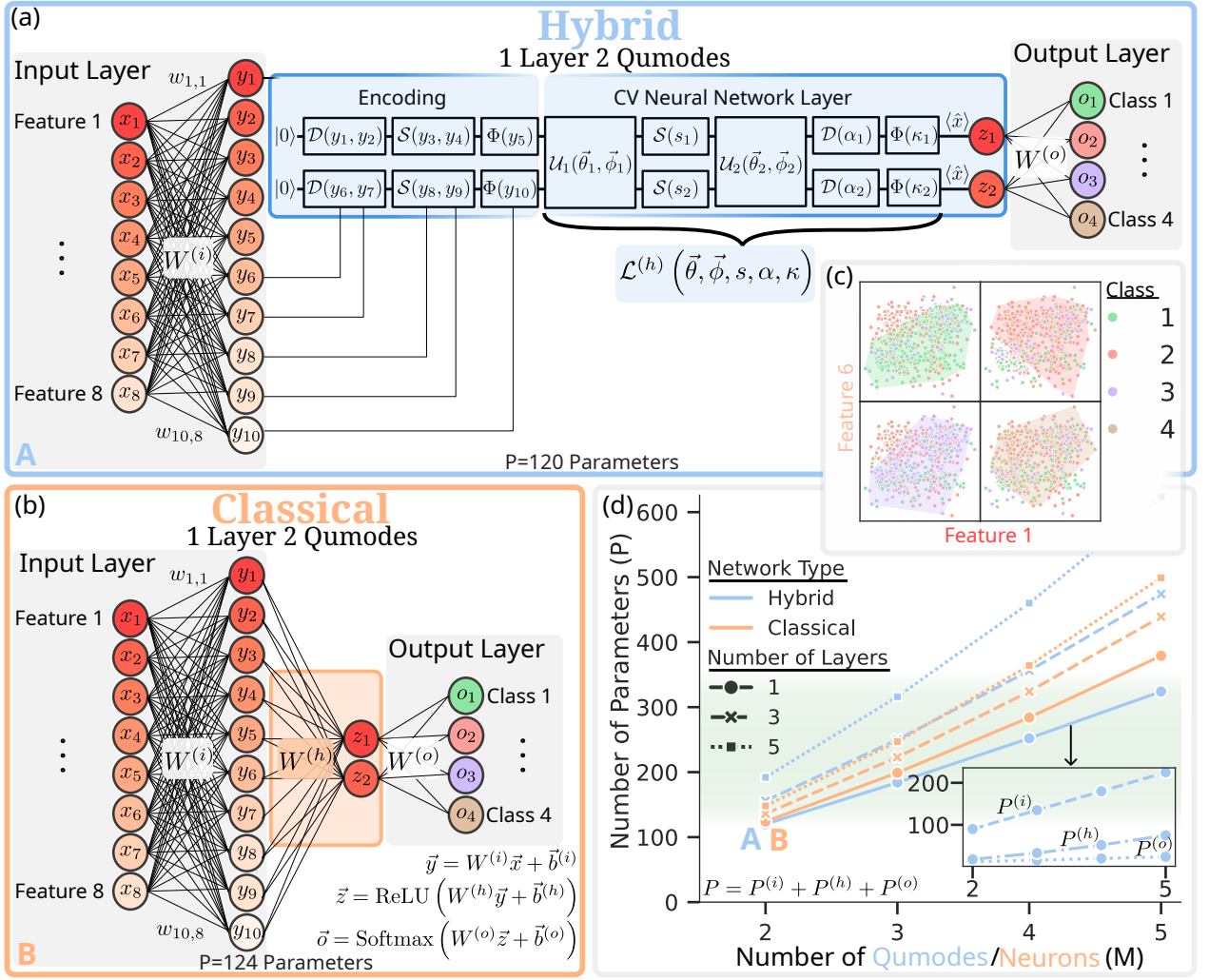


FIG. 1: Summary of hybrid and classical neural network architectures. (a) A one layer two qumode hybrid neural network, network **A**, with input, encoding, CV neural network [15], and output layers. Data is inputted into the classical input layer, outputs from the inputs layer are then inputted into the encoding gates [20, 21]. A single CV neural net layer is labelled as $\mathcal{L}^{(h)}$. This specific network has 120 parameters. The gates in the quantum neural network are described in Section II and Supplementary Section A 1. (b) An equivalent all classical network to the hybrid network, network **B**. Here, the hidden layer, $W^{(h)}$ is a classical layer with two neurons. In the lower right is a mathematical description of operations happening at each layer of the network. This network has 124 parameters. (c) Feature 1 and Feature 6 from the validation set of the classification dataset. The shaded region in each subplot surrounds all the samples of the corresponding class. (d) The number of parameters in both the hybrid and classical networks as a function of the number modes. The inset shows the scaling of the input, hidden, and output layers for the two qumode hybrid network.

for training and 300 for validation) equally distributed between 4 classes, each with 8 features (see Methods VII A). An example of this distribution, for 2 of the 8 features is shown in Fig. 1c, where the area encompassed by each feature in each of the classes is shown by a shaded region. The overlap of these regions demonstrates that it is impossible to classify each sample simply based on 2 features, and explains why all 8 features must be considered. As a consequence, our input layer has 8 neurons, while the output layer contains 4 neurons.

To create a hybrid neural network, the classical hidden

layers ($W^{(h)}$) are replaced with an encoding layer [20, 21] followed by a CV quantum neural network ($\mathcal{L}^{(h)}$, CVQNN) [15], as shown in Fig. 1a. Such CVQNNs can be trained via backpropagation [23] (see Supplementary Section A 3) and they, along with the encoding layer, can be realized with photonic elements on-chip [6, 24–26], meaning that both can be seamlessly integrated with classical photonic neural networks. First, a series of displacement (\mathcal{D}), squeezing (\mathcal{S}) and non-Gaussian Kerr (Φ) gates encodes the classical information into quantum modes (qumodes) (see Supplementary Section A 1

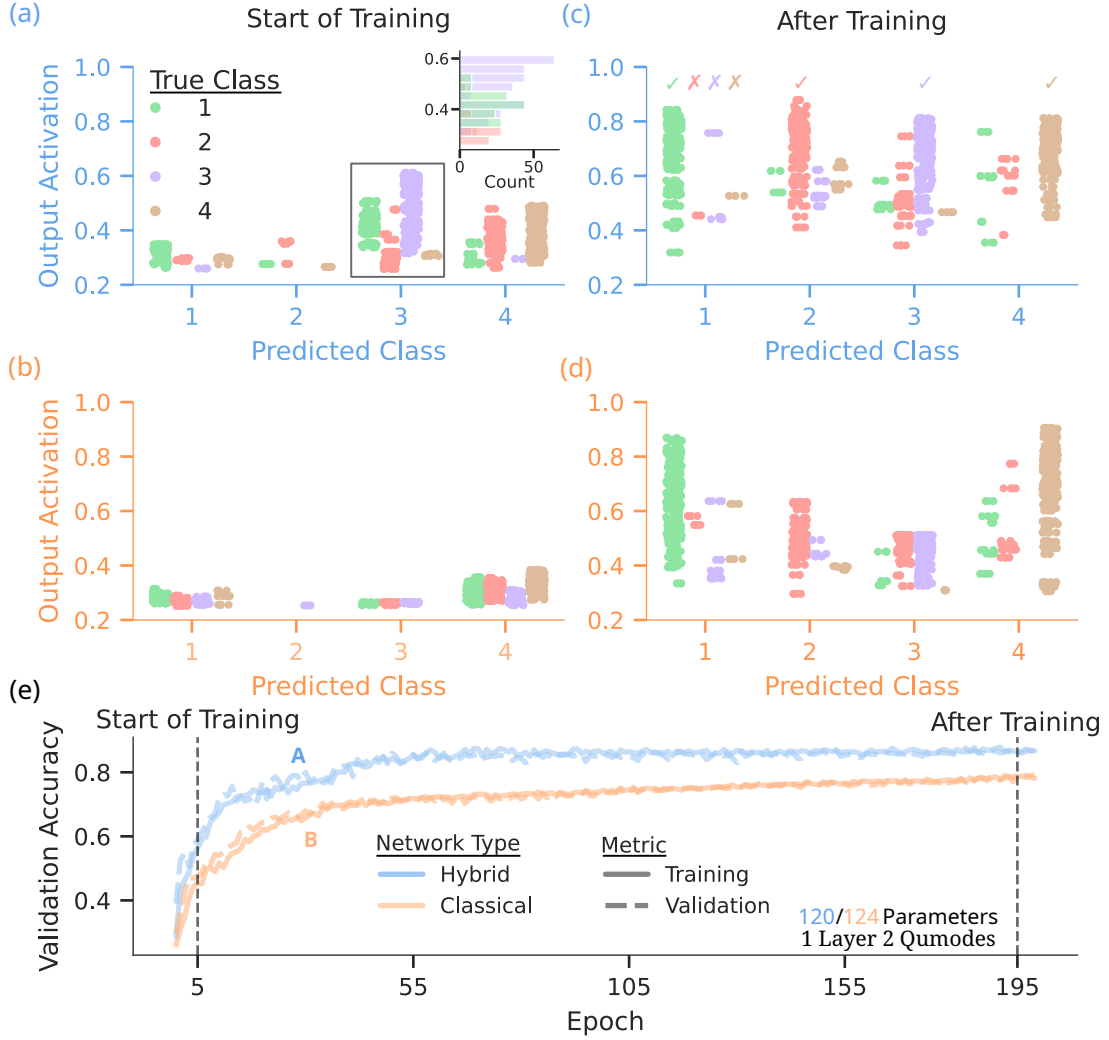


FIG. 2: Demonstration of hybrid and classical networks learning to classify the synthetically generated dataset. (a) The maximum output activations for an untrained 120 parameter hybrid network, network **A**. The x-axis is the class the network predicted while the colour corresponds to the true class. The inset shows the maximum output activations for all samples predicted as class three. (b) The maximum output activation for an untrained 124 parameter network **B**. (c) The maximum output activations for network **A** after it has been trained (d) The maximum output activations for a trained network **B**. (e) The training and validation accuracy curves for network **A** and **B**.

for more information on the quantum gates.) Note that the Kerr gates provide a non-linearity that, while difficult to simulate classically, results in highly trainable and more performant networks [27].

Once encoded into qumodes, the information flows through the CVQNN, before exiting through the classical output layer. As shown in Fig. 1a, the CVQNN is comprised of \mathcal{D} , \mathcal{S} and Φ gates, parameterized by s , α and κ , respectively, interspersed with linear interferometers \mathcal{U} that are controlled by a set of phase shifters, $\vec{\theta}_i$ and $\vec{\phi}_i$, that can be used to perform any unitary operation on the qumodes. Altogether, s , α , κ , $\vec{\theta}$ and $\vec{\phi}$ are the parameters of the CVQNN that, together, with the weights of the classical input and output layers, are

trained using conventional gradient descent.

In sum, each network is characterized by P parameters, which depend on its type and geometry. For a classical network, this is simply the number of weights in weight matrix W and bias vector b summed over all layers. In contrast, for a hybrid network,

$$P = 5M(I+1) + L(M(M-1) + 7M) + O(M+1), \quad (1)$$

where I is the input dimension, M is the number of qumodes, L is the number of layers, and O is the output dimension. Here, the first and third terms represent the number of parameters in the input and output layers, while the middle term is the number of parameters in the quantum layer. Fig. 1d shows the scaling of P as a

function of the number of qumodes in the CVQNN (hidden classical layer), for 1-, 3- and 5-layer networks. For this range, it is possible to find both classical and hybrid networks with P ranging between about 100 and 600. We are therefore able to identify both types of networks with similar number of parameters (and hence, expected complexity) and, in what follows, we set out to compare their performance.

III. TRAINING AND VALIDATION

We begin by constructing models of the neural networks, implementing classical layers in Tensorflow [28] and quantum layers using PennyLane and Strawberryfields [29, 30] (see Methods VII C and VII B). We assess each network accuracy, before, during and after training, by comparing the class that it assigns (i.e., output neuron o_i with the highest activation) to each of the 700 training (or 300 validation) samples. The overall network accuracy is the number of correct classifications over the size of the training (validation) set.

As an example, we consider the accuracy of a 120 and 124 parameter hybrid and classical neural network, corresponding to the 1-layer, 2-qumode and 2-hidden neuron networks shown in Fig. 1a and b, respectively. We first show how well the hybrid network can classify the validation set at the start of the training, plotting the predicted class for each sample (color coded by the true class) along with the success probability assigned (i.e., value of the highest output neuron). We observe an almost-random distribution of true class vs. predicted class for the unoptimized hybrid network, with an overall accuracy of only 0.58. Similarly, the maximum output activation for this unoptimized hybrid network is poor, peaking at 0.61 for class 3 (see inset), but generally well-below 0.4. That is, before training, the hybrid network is both ‘hesitant’ and inaccurate. The results of the untrained classical network, shown in Fig. 2b, are qualitatively similar but poorer, with an overall accuracy of only 0.47 and peak output probability of 0.38.

We train the network parameters over 200 epochs, updating the weights 22 times per epoch. We calculate the network accuracy after each epoch, using both the training (solid curves) and validation (dashed curves) sets, showing the results for both exemplary networks in Fig. 2e. Note that the overlay of the curves indicates that there is no overfitting. As expected, the network accuracy increase, reaching 0.87 and 0.79 for the hybrid and classical systems, demonstrating the advantage of incorporating quantum layers.

The advantage of incorporating quantum layers can be seen more clearly when considering the classification performance for both hybrid and classical networks after training (at epoch 195), shown in Fig. 2c and d, respectively. The hybrid network consistently classifies all samples correctly, with a maximal probability output over 0.80 across all 4 classes. In contrast, while the fully

classical network identifies class 1 and 4 samples, with output probabilities reaching 0.91, it struggles with class 2 and 3 samples. For class 3 samples, in particular, the trained fully-classical network is already outperformed by the untrained hybrid network.

IV. LARGER NETWORKS

To more fully explore the difference between hybrid and classical photonic neural networks, we repeat our analysis of the previous section with networks of varying qumodes/neurons and layers (c.f., Fig. 1d). In total we train 342 hybrid networks and 518 classical networks, split in groups of 10 to 30 (hybrid) and 20 (classical) in sizes that range from 69 to 590 parameters. For the classical devices, this corresponds to roughly single-layer 8×8 and 24×24 classical networks. To determine a threshold for well trained networks a non-probabilistic linear support vector machine was fit to the data achieving an accuracy of 0.72 (see Supplementary Section A 7. Neural networks above this threshold are considered well-trained, while any network with an accuracy around 0.25 is considered failed (as a random selection should result in an accuracy of 0.25). The aggregate results for the 120 (hybrid) and 124 (classical) parameter networks are shown in Fig. 3a. This result further reinforces the power of the quantum layers, as it makes clear that many more highly accurate hybrid networks are trained than classical ones. More specifically, the average well-trained hybrid network has an accuracy of 0.85 ± 0.01 while the fully classical networks have an average accuracy of only 0.79 ± 0.03 , where the larger variance directly follows from the difficulty of training. In fact, for this network size, only 6.9% of hybrid networks had an average accuracy below 72% and none failed in training, in contrast with the 50% of classical networks with an accuracy below the threshold. and the 4.2% that failed. That is, as expected, the network performance and trainability significantly improves due to an increased informational capacity and improved optimization landscape [27].

We repeat this analysis for all network sizes and present the results in Fig. 3c. Here, we observe that for all networks with 316 parameters or less, the average accuracy of the well-trained hybrid networks exceeds that of the classical networks, while the accuracy distribution for the hybrid networks remains much smaller than that of the classical devices. Hybrid networks were also much more likely to optimize beyond the 0.72 accuracy threshold, with 95.9% of all trained hybrid networks reaching this threshold compared to the 76.3% of classical networks (the rate of poorly trained networks can be seen in Fig.3b). This further indicates that hybrid networks are much more likely to optimize successfully. More so, the average accuracy of 0.85 ± 0.03 for the 120 parameter hybrid network is only matched by classical networks at 235 parameters (0.86 ± 0.04). That is, the inclusion of quantum layers consistently allows smaller hybrid networks

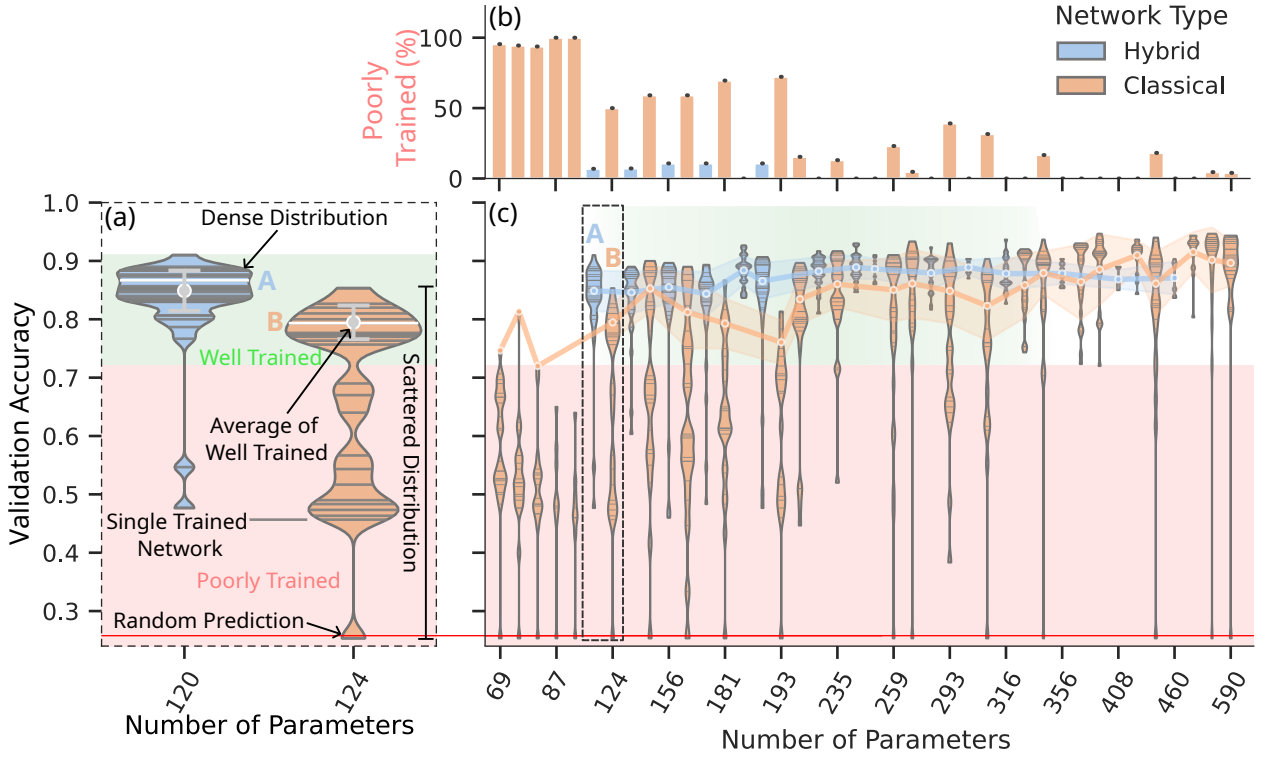


FIG. 3: Statistical violin plots of all hybrid and classical networks trained. (a) Annotated violins of the 120 parameter hybrid network and 124 parameter classical network. Shaded blue and orange region shows the region of well trained networks that scored better than 72% (accuracy of linear support vector machine model). The point on each violin is the average of the well trained networks with the error bars showing one standard deviation on this mean. The red shaded region are considered poorly trained networks while networks below the solid red failed to optimize at all. The white line is networks **A** and **B** seen in Fig. 2 and Fig. 1ab. (c) Violin plot of all networks trained in this study. Each violin is a statistical fit (kernel density estimation) of all networks with a given number of parameters where each grey horizontal line is the maximum accuracy of one network during training. The line is the mean of the upper of the well trained networks networks and the shaded region is the standard deviation on that mean. (b) Bar plot showing the percentage of networks which failed to beat the non-probabilistic linear model (< 72% accuracy, poorly trained).

to outperform similarly sized classical networks and even those that are significantly larger.

Although Fig. 3c suggests that there is no benefit to including quantum layers for networks with more than 316 parameters, this is likely not true. Rather, this may be a direct consequence of the difficulty of simulating large quantum networks which limits the cutoff dimension for our large CVQNNs to 5 (while smaller networks were simulated up to a cutoff of 11). Since the amount of information that can be encoded into each mode of the network is dependent on this, so will the accuracy of the network (see Supplementary Section A 1 for more details), while also requiring longer optimization times. We note, however, that in contrast to in simulations, experimentally increasing the cutoff dimensions is straightforward.

V. ROBUSTNESS TO NOISE

Photonic neural networks are inherently analog systems of which precision is ultimately limited by noise [31]. This noise comes from a combination of thermal fluctuations, noise in the weight control currents, vibrational changes in input coupling, or detector noise. Regardless of the source, noise will ultimately determine how well a given weight in the neural network can be actuated. For convenient comparison to digital bit precision, noise is often converted to an effective number of bits (ENOB) which is determined according to the Shannon-Hartley theorem as,

$$ENOB = \log_2 \left(1 + \frac{w_{max} - w_{min}}{\sigma} \right). \quad (2)$$

Here, w_{max} and w_{min} are the respective allowed maximum and minimum values of the given weight w , and σ is the standard deviation of the noise on w . Thus, the

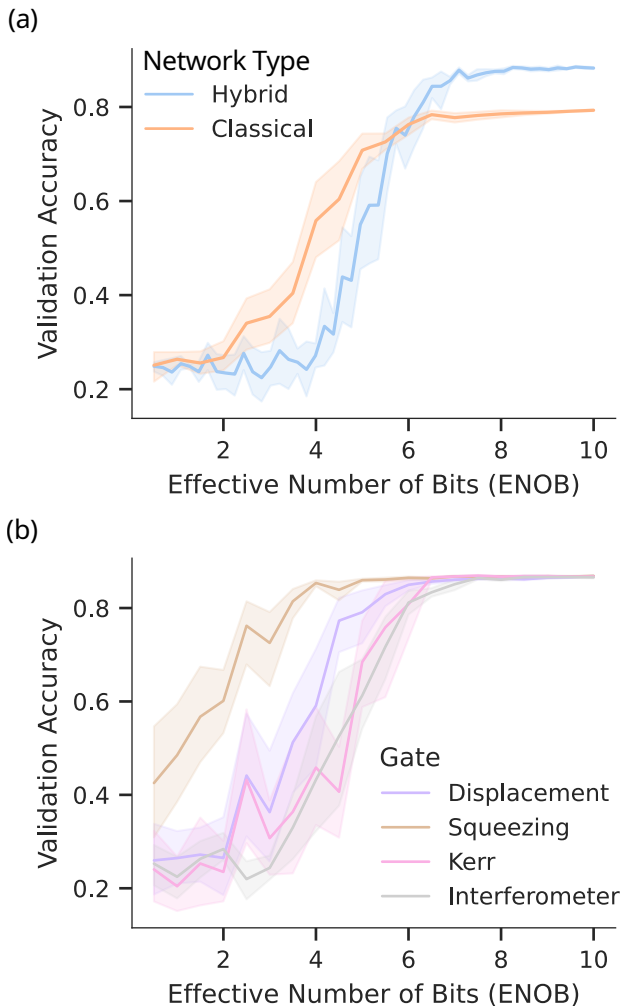


FIG. 4: Analysis of the impact of noise on hybrid and classical network performance. (a) The validation accuracy of a 120 parameter hybrid network and 124 parameter classical network as a function of the ENOB of the parameters. (b) The validation accuracy of a 120 parameter hybrid network with different ENOB on the different gate parameters. Kerr and interferometer gates are the most sensitive to bit precision.

ENOB represents the signal to noise ratio for an analog signal.

For a classical layer of a photonic neural network, all parameters have the range $[w_{min}, w_{max}] = [-1, 1]$ due to optical transmission in a balanced photo detection scheme being fully in one detector, $+1$, or fully in the other detector, -1 [9, 32, 33]. In contrast, a quantum layer has both amplitude and phase parameters, where for phase $[w_{min}, w_{max}] = [0, 2\pi]$ and for amplitude parameters $[w_{min}, w_{max}] = [0, a_{max}]$, where a_{max} is the maximum amplitude parameter in the whole network. Thus, we can choose a σ for the noise and from that calculate the ENOB for the network and, by rerunning our simulations calculate the network accuracy in the presence of noise.

Fig. 4a shows exemplary curves for the network accuracy as a function of the ENOB for both the 120 parameter hybrid network (blue) and the 124 parameter classical network. For each ENOB value, the validation accuracy was calculated ten times for different randomized noise values, with the mean shown by the dark curve and the shaded region representing one standard deviation. The classical network achieves near ideal accuracy, (10% worse than ideal performance) at 5.5 bits of precision while the hybrid network requires 6.3 bits of precision. Both of these values are below the state-of-the-art 9 bits of precision that are achievable with photonic neural networks [34].

Focusing on just the noise in the quantum neural network, we show how the hybrid network accuracy depends on the ENOB of the different gate parameters in Fig. 4b. To achieve near ideal accuracy, in this case 0.78, the displacement, squeezing, kerr, and interferometer gates must have 5.0, 3.5, 6.0, and 5.0 (± 0.5) bits of precision, respectively. This demonstrates that the network performance is most sensitive to the operation of \mathcal{U} , which provides the same functionality as the weights of a classical layer, and Φ , which provides the non-linearity. The relatively low required bit precision on the squeeze gate indicates that the precise magnitude of the squeezing is not important, only that squeezing is present (agreeing with current opinions in the field [35]). Regardless, we observe that the overall network performance is robust in the presence of noise, simply needing to exceed an experimentally feasible value.

VI. DISCUSSION AND CONCLUSION

Here, we have shown that hybrid neural networks based on the continuous variable quantum formalism could provide real performance and trainability benefits over fully classical networks of the same size, providing a route to increased complexity with fewer photonic resources. As an example, we showed that for a complex classification task, a small hybrid network with 120 trainable parameters achieved an average well trained accuracy of 0.85 ± 0.03 , similar in performance to a much larger 235 parameter classical network. Across a range of network sizes, the hybrid networks were always more trainable and in most cases achieved greater performance. Encouragingly, hybrid network achieved peak performance with only 6.3 effective bits of precision, well within the capabilities of current photonic platforms [8, 34]. We expect that such networks could also be trained with noise present to explore the performance benefits of noise aware training.

Hybrid networks, such as we envision, are implementable on a integrated photonic platform and would also be directly compatible with existing photonic communication platforms [6, 36]. While we focused on a classification task, it is clear that they could be applied to realize other functionalities. For example, in conjunc-

tion with direct integration to existing communication platforms, hybrid networks have potential applications in quantum repeaters [37] and photonic edge computing [38]. Scaling to larger and more complex neural networks is a requirement to solve difficult computational tasks often seen in these applications. Typically, several multiplexing approaches such as wavelength, time, and spatial division multiplexing are used to provide denser processing, thereby increasing the number of parameters, and adding more computational power [39]. However, multiplexing approaches have drawbacks such as slower speeds, larger footprints, and more complicated electrical control. Here we have shown that hybrid networks provide an additional approach to scale network complexity and solve more difficult computational tasks with fewer parameters.

VII. METHODS

A. Synthetic Dataset

Data was generated using the Scikit-Learn [22] `make_classification()` function. As mentioned in the text, this dataset featured 8 inputs, 4 classes, and 1000 samples. All features were informative, meaning they included non-redundant information, and each class featured 3 clusters of datapoints. On average, the clusters of datapoints were separated by an eight dimensional vector of length 3.0 (the default is 1). 2% of samples were assigned a random class to increase difficulty. The dataset was normalized to the domain $[0, 1]$ prior to training to simulate input transmission seen in photonic circuits [33]. The random state to generate this data can be provided upon request.

B. Classical Model

The classical models (and layers) were implemented in the Tensorflow framework. ReLU non-linearities were used between each of the classical layers. All classical layers were implemented using Keras Dense layers with weight clipping beyond the domain $[-1, 1]$ [33]. This simulated the range of transmission values available on photonic hardware. The size of the classical hidden layers was determined using an algorithm which, for each classical layer, matched the number of parameters in the corresponding layer of the hybrid network. In this way, both the total number of layers (circuit depth) and total number of parameters were equivalent. The final output of the network used a softmax non-linearity to convert the output activations to a probability distribution for classification.

C. Hybrid Model

The hybrid models were fully implemented in the Tensorflow framework [28] with the PennyLane quantum machine learning Tensorflow interface [29] and the Strawberryfields Tensorflow based simulator [30]. This avoided array conversions between different frameworks and enabled automated gradient calculations, GPU support, and access to machine learning functions. A Fock basis simulator was used as it can simulate the non-gaussian gate ($\hat{O} \sim e^{\hat{n}^2}$) as in non-linear activation function. The Fock simulator, fully implemented in Tensorflow, records the amplitudes for each of the photon number states in the Fock basis as gates are applied. The cutoff dimension D specifies the number of Fock states simulated ($|0\rangle, |1\rangle, \dots, |D-1\rangle$) and therefore size of the state space (see Supplementary Section A 1). The total number of states simulated is given by D^N where N is the number of qumodes.

Data begins at the input layer which, unlike the classical network, had no non-linearity. After the input layer, is the encoding layer into the quantum circuit. The encoding layer accepts 5 inputs for each qumode in the circuit. An amplitude and phase for the squeeze gate, an amplitude and phase for the displacement gate, and an amplitude and phase for the kerr non-linearity. The inputs into the encoding layer are scaled to the domain $[0, 2\pi]$, for phase parameters, and to $[0, a_{max}]$, for amplitude parameters, using the following functions:

$$\tilde{y}_i^{(amplitude)} = a_{max} \text{Sig}(y_i)$$

$$\tilde{y}_j^{(phase)} = 2\pi \text{Sig}(y_j)$$

Where $\tilde{y}_{\{i,j\}}^{(amplitude, phase)}$ is the scaled value, $\text{Sig}(y)$ is the sigmoid function, a_{max} is the maximum displacement/squeezing amplitude, and $y_{\{i,j\}}$ is the output from the previous layer. a_{max} was determined using a brute force method outlined in Supplementary Section A 2. Acting on this encoded state is the CV quantum neural network layer made up of N-port interferometers ($\mathcal{U}_1, \mathcal{U}_2$), squeezing gates (\mathcal{S}), displacement gates (\mathcal{D}), and Kerr non-linearities (Φ). First sequence of gates, $\mathcal{U}_2 \mathcal{S} \mathcal{U}_1$, represents the matrix multiplication step, the displacement gate \mathcal{D} represents the bias, and the kerr non-linearity Φ acts as the activation function [15]. The amplitude parameters were initialized uniformly on the domain $[0, a_{max}]$ and phase parameters on the domain $[0, 2\pi]$. All amplitude values were L1 regularized to improve state normalization during training. For mathematical and graphical descriptions of these gates refer to Supplementary Section A 1. Models with 2-4 qumodes and 1-5 layers were trained. Homodyne detection in the position basis (\hat{x}) is used to measure the output value of each of the qumodes. These measurements are then inputted into the final classical output layer which is used to make a classification.

D. Training

All networks were trained using conventional gradient descent and backpropagation. The Adam optimizer with a learning rate of $\eta = 0.001$ was used with a batch size of 32. A categorical cross entropy loss function was used to calculate the loss as this is a multi class classification task. 10-30 hybrid networks (three different cutoff dimension values, 10 for each cutoff) and 20 classical were trained for each network size. Training was conducted on the Digital Research Alliance of Canada's Graham cluster.

VIII. ACKNOWLEDGMENTS

All authors acknowledge the support of the Natural Sciences and Engineering Research Council of Canada

(NSERC), Digital Research Alliance of Canada (DRAC), and Queen's University. TA and BJS acknowledge the support of the Vector Institute. BJS is supported by the Canada Research Chairs program. NR and BJS acknowledge the support of the Canadian Foundation for Innovation (CFI).

IX. AUTHOR CONTRIBUTIONS

The project was originally conceived by TA and BJS. AH provided initial code and, with SB, useful discussion. TA performed all simulations to generated data and figured. TA prepared the original manuscript which was edited by BJS and NR. Research led by BJS and NR.

-
- [1] Bhavin J. Shastri, Alexander N. Tait, T. Ferreira de Lima, Wolfram H. P. Pernice, Harish Bhaskaran, C. D. Wright, and Paul R. Prucnal. Photonics for artificial intelligence and neuromorphic computing. 15(2):102–114. ISSN 1749-4885, 1749-4893. doi:10.1038/s41566-020-00754-y. URL <http://www.nature.com/articles/s41566-020-00754-y>.
 - [2] Weipeng Zhang, Joshua C. Lederman, Thomas Ferreira de Lima, Jiawei Zhang, Simon Bilodeau, Leila Hudson, Alexander Tait, Bhavin J. Shastri, and Paul R. Prucnal. A system-on-chip microwave photonic processor solves dynamic RF interference in real time with picosecond latency. 13(1):14. ISSN 2047-7538. doi:10.1038/s41377-023-01362-5. URL <https://www.nature.com/articles/s41377-023-01362-5>. Publisher: Nature Publishing Group.
 - [3] Hailong Zhou, Jianji Dong, Junwei Cheng, Wenchan Dong, Chaoran Huang, Yichen Shen, Qiming Zhang, Min Gu, Chao Qian, Hongsheng Chen, Zhichao Ruan, and Xinliang Zhang. Photonic matrix multiplication lights up photonic accelerator and beyond. 11(1):30. ISSN 2047-7538. doi:10.1038/s41377-022-00717-8. URL <https://www.nature.com/articles/s41377-022-00717-8>. Publisher: Nature Publishing Group.
 - [4] Muhammad Kashif and Saif Al-Kuwari. Design space exploration of hybrid quantum–classical neural networks. 10(23). ISSN 2079-9292. doi:10.3390/electronics10232980. URL <https://www.mdpi.com/2079-9292/10/23/2980>.
 - [5] Yichen Shen, Nicholas C. Harris, Scott Skirlo, Mihika Prabhu, Tom Baehr-Jones, Michael Hochberg, Xin Sun, Shijie Zhao, Hugo Larochelle, Dirk Englund, and Marin Soljačić. Deep learning with coherent nanophotonic circuits. 11(7):441–446. ISSN 1749-4893. doi:10.1038/nphoton.2017.93. URL <https://www.nature.com/articles/nphoton.2017.93>. Publisher: Nature Publishing Group.
 - [6] J. M. Arrazola, V. Bergholm, K. Brádler, T. R. Bromley, M. J. Collins, I. Dhand, A. Fumagalli, T. Gerits, A. Goussev, L. G. Helt, J. Hundal, T. Isacsson, R. B. Israel, J. Izaac, S. Jahangiri, R. Janik, N. Killo-ran, S. P. Kumar, J. Lavoie, A. E. Lita, D. H. Mahler, M. Menotti, B. Morrison, S. W. Nam, L. Neuhaus, H. Y. Qi, N. Quesada, A. Repeatingon, K. K. Sabapathy, M. Schuld, D. Su, J. Swinerton, A. Száva, K. Tan, P. Tan, V. D. Vaidya, Z. Vernon, Z. Zabaneh, and Y. Zhang. Quantum circuits with many photons on a programmable nanophotonic chip. 591(7848):54–60. ISSN 1476-4687. doi:10.1038/s41586-021-03202-1. URL <https://www.nature.com/articles/s41586-021-03202-1>. Publisher: Nature Publishing Group.
 - [7] Kun Liao, Chentong Li, Tianxiang Dai, Chuyu Zhong, Hongtao Lin, Xiaoyong Hu, and Qihuang Gong. Matrix eigenvalue solver based on reconfigurable photonic neural network. 11(17):4089–4099. ISSN 2192-8614. doi:10.1515/nanoph-2022-0109. URL <https://www.degruyter.com/document/doi/10.1515/nanoph-2022-0109/html?lang=en>. Publisher: De Gruyter.
 - [8] Farshid Ashtiani, Alexander J. Geers, and Firooz Aftouni. An on-chip photonic deep neural network for image classification. 606(7914):501–506. ISSN 1476-4687. doi:10.1038/s41586-022-04714-0. URL <https://www.nature.com/articles/s41586-022-04714-0>. Publisher: Nature Publishing Group.
 - [9] Alexander N. Tait, Thomas Ferreira de Lima, Ellen Zhou, Allie X. Wu, Mitchell A. Nahmias, Bhavin J. Shastri, and Paul R. Prucnal. Neuromorphic photonic networks using silicon photonic weight banks. 7(1):7430. ISSN 2045-2322. doi:10.1038/s41598-017-07754-z. URL <https://www.nature.com/articles/s41598-017-07754-z>. Number: 1 Publisher: Nature Publishing Group.
 - [10] Lorenzo De Marinis and Nicola Andriolli. Photonic integrated neural network accelerators. In *Photonics in Switching and Computing 2021 (2021)*, paper W3B.1, page W3B.1. Optica Publishing Group. doi:10.1364/PSC.2021.W3B.1. URL <https://opg.optica>.

- org/abstract.cfm?uri=PSC-2021-W3B.1.
- [11] Zhongjin Lin, Bhavin J. Shastri, Shangxuan Yu, Jingxiang Song, Yuntao Zhu, Arman Safarnejadian, Wangning Cai, Yanmei Lin, Wei Ke, Mustafa Hammood, Tianye Wang, Mengyue Xu, Zibo Zheng, Mohammed Al-Qadasi, Omid Esmaeeli, Mohamed Rahim, Grzegorz Pakulski, Jens Schmid, Pedro Barrios, Weihong Jiang, Hugh Morrison, Matthew Mitchell, Xiaogang Qiang, Xun Guan, Nicolas A. F. Jaeger, Leslie A. n Rusch, Sudip Shekhar, Wei Shi, Siyuan Yu, Xinlun Cai, and Lukas Chrostowski. 65 GOPS/neuron photonic tensor core with thin-film lithium niobate photonics. URL <http://arxiv.org/abs/2311.16896>.
 - [12] Paul R. Prucnal and Bhavin J. Shastri. *Neuromorphic Photonics*. CRC Press. ISBN 978-1-4987-2524-8. Google-Books-ID: VbvODgAAQBAJ.
 - [13] Alexander Norman Tait. Silicon photonic neural networks. URL <https://dataspace.princeton.edu/handle/88435/dsp01vh53wz43k>. Accepted: 2018-04-26T18:46:40Z Publisher: Princeton, NJ : Princeton University.
 - [14] Peter L. McMahon. The physics of optical computing. 5(12):717–734. ISSN 2522-5820. doi:10.1038/s42254-023-00645-5. URL <https://www.nature.com/articles/s42254-023-00645-5>. Publisher: Nature Publishing Group.
 - [15] Nathan Killoran, Thomas R. Bromley, Juan Miguel Arrazola, Maria Schuld, Nicolás Quesada, and Seth Lloyd. Continuous-variable quantum neural networks. 1(3): 033063, . doi:10.1103/PhysRevResearch.1.033063. URL <https://link.aps.org/doi/10.1103/PhysRevResearch.1.033063>. Publisher: American Physical Society.
 - [16] Sophie Choe. Continuous variable quantum MNIST classifiers. URL <http://arxiv.org/abs/2204.01194>.
 - [17] Shikha Bangar, Leanto Sunny, Kübra Yeter-Aydeniz, and George Siopsis. Experimentally realizable continuous-variable quantum neural networks. 108(4):042414. doi: 10.1103/PhysRevA.108.042414. URL <https://link.aps.org/doi/10.1103/PhysRevA.108.042414>. Publisher: American Physical Society.
 - [18] Lars S. Madsen, Fabian Laudenbach, Mohsen Falamarzi Askarani, Fabien Rortais, Trevor Vincent, Jacob F. F. Bulmer, Filippo M. Miatto, Leonhard Neuhaus, Lukas G. Helt, Matthew J. Collins, Adriana E. Lita, Thomas Gerrits, Sae Woo Nam, Varun D. Vaidya, Matteo Menotti, Ish Dhand, Zachary Vernon, Nicolás Quesada, and Jonathan Lavoie. Quantum computational advantage with a programmable photonic processor. 606 (7912):75–81. ISSN 1476-4687. doi:10.1038/s41586-022-04725-x. URL <https://www.nature.com/articles/s41586-022-04725-x>. Number: 7912 Publisher: Nature Publishing Group.
 - [19] Saumil Bandyopadhyay, Alexander Sludds, Stefan Krastanov, Ryan Hamerly, Nicholas Harris, Darius Bunandar, Matthew Shreshinsky, Michael Hochberg, and Dirk Englund. Single chip photonic deep neural network with accelerated training. URL <http://arxiv.org/abs/2208.01623>.
 - [20] Maria Schuld and Nathan Killoran. Quantum machine learning in feature hilbert spaces. 122(4):040504. doi: 10.1103/PhysRevLett.122.040504. URL <https://link.aps.org/doi/10.1103/PhysRevLett.122.040504>. Publisher: American Physical Society.
 - [21] Vojtěch Havlíček, Antonio D. Córcoles, Kristan Temme, Aram W. Harrow, Abhinav Kandala, Jerry M. Chow, and Jay M. Gambetta. Supervised learning with quantum-enhanced feature spaces. 567(7747):209–212. ISSN 1476-4687. doi:10.1038/s41586-019-0980-2. URL <https://www.nature.com/articles/s41586-019-0980-2>. Publisher: Nature Publishing Group.
 - [22] Fabian Pedregosa, Gaël Varoquaux, Alexandre Gramfort, Vincent Michel, Bertrand Thirion, Olivier Grisel, Mathieu Blondel, Peter Prettenhofer, Ron Weiss, Vincent Dubourg, Jake Vanderplas, Alexandre Passos, David Cournapeau, Matthieu Brucher, Matthieu Perrot, and Édouard Duchesnay. Scikit-learn: Machine learning in python. 12(85):2825–2830. ISSN 1533-7928. URL <http://jmlr.org/papers/v12/pedregosa11a.html>.
 - [23] Gavin E. Crooks. Gradients of parameterized quantum gates using the parameter-shift rule and gate decomposition. URL <http://arxiv.org/abs/1905.13311>.
 - [24] V. D. Vaidya, B. Morrison, L. G. Helt, R. Shahrokhshahi, D. H. Mahler, M. J. Collins, K. Tan, J. Lavoie, A. Reppingon, M. Menotti, N. Quesada, R. C. Pooser, A. E. Lita, T. Gerrits, S. W. Nam, and Z. Vernon. Broadband quadrature-squeezed vacuum and nonclassical photon number correlations from a nanophotonic device. 6(39): eaba9186. doi:10.1126/sciadv.aba9186. URL <https://www.science.org/doi/10.1126/sciadv.aba9186>. Publisher: American Association for the Advancement of Science.
 - [25] Y. Zhang, M. Menotti, K. Tan, V. D. Vaidya, D. H. Mahler, L. G. Helt, L. Zatti, M. Liscidini, B. Morrison, and Z. Vernon. Squeezed light from a nanophotonic molecule. 12(1):2233, . ISSN 2041-1723. doi:10.1038/s41467-021-22540-2. URL <https://www.nature.com/articles/s41467-021-22540-2>. Number: 1 Publisher: Nature Publishing Group.
 - [26] A. I. Lvovsky and M. G. Raymer. Continuous-variable optical quantum-state tomography. 81 (1):299–332. ISSN 0034-6861, 1539-0756. doi: 10.1103/RevModPhys.81.299. URL <https://link.aps.org/doi/10.1103/RevModPhys.81.299>.
 - [27] Amira Abbas, David Sutter, Christa Zoufal, Aurelien Lucchi, Alessio Figalli, and Stefan Woerner. The power of quantum neural networks. 1(6):403–409. ISSN 2662-8457. doi:10.1038/s43588-021-00084-1. URL <https://www.nature.com/articles/s43588-021-00084-1>. Publisher: Nature Publishing Group.
 - [28] Martín Abadi, Paul Barham, Jianmin Chen, Zhifeng Chen, Andy Davis, Jeffrey Dean, Matthieu Devin, Sanjay Ghemawat, Geoffrey Irving, Michael Isard, Manjunath Kudlur, Josh Levenberg, Rajat Monga, Sherry Moore, Derek G. Murray, Benoit Steiner, Paul Tucker, Vijay Vasudevan, Pete Warden, Martin Wicke, Yuan Yu, and Xiaoqiang Zheng. TensorFlow: A system for large-scale machine learning. URL <http://arxiv.org/abs/1605.08695>.
 - [29] Ville Bergholm, Josh Izaac, Maria Schuld, Christian Gogolin, Shahnawaz Ahmed, Vishnu Ajith, M. Sohaib Alam, Guillermo Alonso-Linares, B. AkashNarayanan, Ali Asadi, Juan Miguel Arrazola, Utkarsh Azad, Sam Banning, Carsten Blank, Thomas R. Bromley, Benjamin A. Cordier, Jack Ceroni, Alain Delgado, Olivia Di Matteo, Amintor Dusko, Tanya Garg, Diego Guala, Anthony Hayes, Ryan Hill, Aroosa Ijaz, Theodor Isacson, David Ittah, Soran Jahangiri, Prateek Jain, Ed-

- ward Jiang, Ankit Khandelwal, Korbinian Kottmann, Robert A. Lang, Christina Lee, Thomas Loke, Angus Lowe, Keri McKiernan, Johannes Jakob Meyer, J. A. Montañez-Barrera, Romain Moyard, Zeyue Niu, Lee James O’Riordan, Steven Oud, Ashish Panigrahi, Chae-Yeun Park, Daniel Polatajko, Nicolás Quesada, Chase Roberts, Nahum Sá, Isidor Schoch, Borun Shi, Shuli Shu, Sukin Sim, Arshpreet Singh, Ingrid Strandberg, Jay Soni, Antal Száva, Slimane Thabet, Rodrigo A. Vargas-Hernández, Trevor Vincent, Nicola Vitucci, Maurice Weber, David Wierichs, Roeland Wiersema, Moritz Willmann, Vincent Wong, Shaoming Zhang, and Nathan Killoran. PennyLane: Automatic differentiation of hybrid quantum-classical computations. URL <http://arxiv.org/abs/1811.04968>.
- [30] Nathan Killoran, Josh Izaac, Nicolás Quesada, Ville Bergholm, Matthew Amy, and Christian Weedbrook. Strawberry fields: A software platform for photonic quantum computing. 3:129, . ISSN 2521-327X. doi: 10.22331/q-2019-03-11-129. URL <http://arxiv.org/abs/1804.03159>.
- [31] Thomas Ferreira de Lima, Alexander N. Tait, Hooman Saeidi, Mitchell A. Nahmias, Hsuan-Tung Peng, Siamak Abbaslou, Bhavin J. Shastri, and Paul R. Prucnal. Noise analysis of photonic modulator neurons. 26(1):1–9. ISSN 1558-4542. doi:10.1109/JSTQE.2019.2931252. URL <https://ieeexplore.ieee.org/document/8782580>.
- [32] Alexander N. Tait, Mitchell A. Nahmias, Bhavin J. Shastri, and Paul R. Prucnal. Broadcast and weight: An integrated network for scalable photonic spike processing. 32(21):4029–4041, . ISSN 1558-2213. doi: 10.1109/JLT.2014.2345652. URL <https://ieeexplore.ieee.org/document/6872524>. Conference Name: Journal of Lightwave Technology.
- [33] Viraj Bangari, Bicky Marquez, Heidi Miller, A.N. Tait, Mitchell Nahmias, Thomas Ferreira de Lima, Hsuan-Tung Peng, Paul Prucnal, and Bhavin Shastri. Digital electronics and analog photonics for convolutional neural networks (DEAP-CNNs). PP:1–1. doi: 10.1109/JSTQE.2019.2945540.
- [34] Weipeng Zhang, Chaoran Huang, Hsuan-Tung Peng, Simon Bilodeau, Aashu Jha, Eric Blow, Thomas Ferreira de Lima, Bhavin J. Shastri, and Paul Prucnal. Silicon microring synapses enable photonic deep learning beyond 9-bit precision. 9(5):579–584, . ISSN 2334-2536. doi: 10.1364/OPTICA.446100. URL <https://opg.optica.org/optica/abstract.cfm?uri=optica-9-5-579>.
- [35] Olivier Pfister. Continuous-variable quantum computing in the quantum optical frequency comb. 53(1):012001. ISSN 0953-4075. doi:10.1088/1361-6455/ab526f. URL <https://dx.doi.org/10.1088/1361-6455/ab526f>. Publisher: IOP Publishing.
- [36] Vicente Martin, Juan Pedro Brito, Carmen Escribano, Marco Menchetti, Catherine White, Andrew Lord, Felix Wissel, Matthias Gunkel, Paulette Gavignet, Naveena Genay, Olivier Le Mout, Carlos Abellán, Antonio Manzalini, Antonio Pastor-Perales, Victor López, and Diego López. Quantum technologies in the telecommunications industry. 8(1):19. ISSN 2662-4400, 2196-0763. doi:10.1140/epjqt/s40507-021-00108-9. URL <https://epjquantumtechnology.springeropen.com/articles/10.1140/epjqt/s40507-021-00108-9>.
- [37] Koji Azuma, Sophia E. Economou, David Elkouss, Paul Hilaire, Liang Jiang, Hoi-Kwong Lo, and Ilan Tzitrin. Quantum repeaters: From quantum networks to the quantum internet. 95(4):045006. doi: 10.1103/RevModPhys.95.045006. URL <https://link.aps.org/doi/10.1103/RevModPhys.95.045006>. Publisher: American Physical Society.
- [38] Alexander Sludds, Saumil Bandyopadhyay, Zaijun Chen, Zhizhen Zhong, Jared Cochrane, Liane Bernstein, Darius Bunandar, P. Ben Dixon, Scott A. Hamilton, Matthew Streshinsky, Ari Novack, Tom Baehr-Jones, Michael Hochberg, Manya Ghobadi, Ryan Hamerly, and Dirk Englund. Delocalized photonic deep learning on the internet’s edge. 378(6617):270–276. doi: 10.1126/science.abq8271. URL <https://www.science.org/doi/10.1126/science.abq8271>. Publisher: American Association for the Advancement of Science.
- [39] Yunping Bai, Xingyuan Xu, Mengxi Tan, Yang Sun, Yang Li, Jiayang Wu, Roberto Morandotti, Arnan Mitchell, Kun Xu, and David J. Moss. Photonic multiplexing techniques for neuromorphic computing. 12(5):795–817. ISSN 2192-8614. doi:10.1515/nanoph-2022-0485. URL <https://www.degruyter.com/document/doi/10.1515/nanoph-2022-0485/html?lang=en>. Publisher: De Gruyter.
- [40] Christian Weedbrook, Stefano Pirandola, Raúl García-Patrón, Nicolas J. Cerf, Timothy C. Ralph, Jeffrey H. Shapiro, and Seth Lloyd. Gaussian quantum information. 84(2):621–669. ISSN 0034-6861, 1539-0756. doi: 10.1103/RevModPhys.84.621. URL <https://link.aps.org/doi/10.1103/RevModPhys.84.621>.
- [41] Pieter Kok and Brendon W. Lovett. *Introduction to Optical Quantum Information Processing*. Cambridge University Press, 1 edition. ISBN 978-0-521-51914-4 978-1-139-19365-8. doi:10.1017/CBO9781139193658. URL <https://www.cambridge.org/core/product/identifier/9781139193658/type/book>.
- [42] C. C. Gerry and Peter Knight. *Introductory quantum optics*. Cambridge University Press. ISBN 978-0-521-82035-6 978-0-521-52735-4.
- [43] Andrew Hayman. Hybrid quantum-classical neural networks with continuous variable quantum computing.
- [44] K. Mitarai, M. Negoro, M. Kitagawa, and K. Fujii. Quantum circuit learning. 98(3):032309. doi: 10.1103/PhysRevA.98.032309. URL <https://link.aps.org/doi/10.1103/PhysRevA.98.032309>. Publisher: American Physical Society.
- [45] Maria Schuld, Ville Bergholm, Christian Gogolin, Josh Izaac, and Nathan Killoran. Evaluating analytic gradients on quantum hardware. 99. doi: 10.1103/PhysRevA.99.032331.

Appendix A: Supplementary Information

1. Simulation and Cutoff Dimension

Simulation of continuous variable quantum circuits can be done in a Gaussian basis or a Fock basis. However, Gaussian simulation is limited to Gaussian operations, operations that map one Gaussian to another [40] or operate linearly with respect to photon number \hat{n} . Gaussian simulation methods are much more efficient on classical computers [30]. By limiting quantum circuits to this reduced linear gate set, there is no quantum advantage and the system is efficiently simulable on a classical computer [41]. To utilize non-linear operations, which are necessary for deep learning and provide computational speedup, the Fock basis simulator must be used as it is capable of simulating $\hat{O} \sim e^{\hat{n}^2}$ [30].

A qumode, essentially a coherent optical state called $|\alpha\rangle$, is a Poissonian superposition of Fock states [42] given by the following.

$$|\alpha\rangle = \sum_n e^{\frac{1}{2}|\alpha|^2} \frac{\alpha^n}{\sqrt{n!}} |n\rangle$$

The Fock simulator works by calculating the probability amplitude of each photon number state as different quantum gates are applied [30]. For example, a displacement operation would shift the Poissonian distribution of Fock states changing the average photon number of a given qumode. A table describing each of the gates used can be seen in Table I. For reference \mathcal{U} is made up of beamsplitter and rotation gates to form an N-port interferometer. In the text the symbol for the kerr gate was Φ while here it is K . Graphical representations plotted in position-momentum phase space can be seen in Fig. 5.

TABLE I: Summary of gates required for CVQNN [43].

Name	Gate	Unitary	Parameters	Gaussian	Modes	Symbol
Displacement	$D(\alpha)$ or $D(a, \theta)$	$\hat{D}(\alpha) = e^{\alpha \hat{a}^\dagger - \alpha^* \hat{a}}$	$\alpha \in \mathbb{C}$ or $a \geq 0, \theta \in [0, 2\pi)$	✓	1	\boxed{D}
Squeezing	$S(s)$ or $S(r, \phi)$	$\hat{S}(z) = e^{(1/2)(z^* \hat{a}^2 - z \hat{a}^{\dagger 2})}$	$z \in \mathbb{C}$ or $r \geq 0, \phi \in [0, 2\pi)$	✓	1	\boxed{S}
Rotation	$R(\theta)$	$\hat{R}(\phi) = e^{-i\phi \hat{n}}$	$\theta \in [0, 2\pi)$	✓	1	\boxed{R}
Beamsplitter	$BS(\theta, \phi)$	$\hat{B}(\theta, \phi) = e^{\theta(e^{i\phi} a_1 a_2^\dagger - e^{-i\phi} a_1^\dagger a_2)}$	$\theta, \phi \in [0, 2\pi)$	✓	2	\boxed{BS}
Kerr	$K(\kappa)$	$\hat{K}(\kappa) = e^{i\kappa \hat{n}^2}$	$\kappa \in [0, 2\pi)$	×	1	\boxed{K}

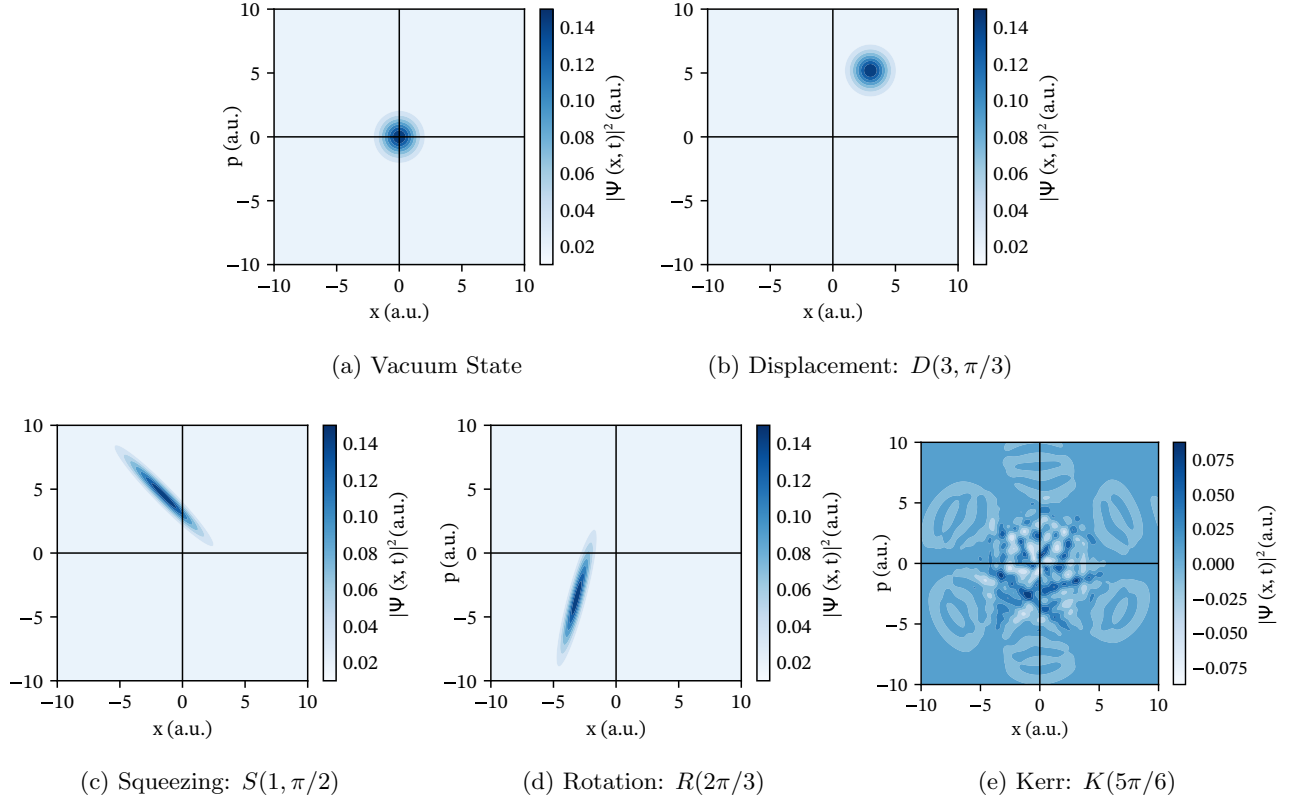


FIG. 5: Phase space diagrams of gate progression from (a)-(e). Taken from [43].

In nature this Fock state distribution can be made up of any state $|0\rangle, |1\rangle, \dots |\infty\rangle$. A computer is not capable of storing the probability amplitude of an infinite number of states so a cutoff dimension, D , is defined. This approximate coherent state is then given by:

$$|\alpha\rangle \approx \sum_n^D e^{\frac{1}{2}|\alpha|^2} \frac{\alpha^n}{\sqrt{n!}} |n\rangle$$

The cutoff dimension then dictates the size of the space and therefore the number available states a qumode can take. Referring to a coherent state $|\alpha\rangle$, where α has previously been defined as a complex parameter, we can define this parameter as a magnitude and phase $\alpha = |\alpha|e^{i\theta}$. The magnitude squared is equal to the average photon number $|\alpha|^2 = \langle \hat{n} \rangle$. Due to this relationship between the magnitude of a coherent state and the average photon number, the maximum state amplitude is tied to the amplitudes of the photon number states. Therefore the cutoff dimension indirectly dictates the size of the state space.

Probability amplitudes of the Fock states $P(\alpha, n) = |\langle \alpha | 0 \rangle|^2, |\langle \alpha | 1 \rangle|^2, \dots, |\langle \alpha | D-1 \rangle|^2$ are stored and changed when applying gates. During simulation the Poisson distribution of Fock states can drift beyond the cutoff dimension denormalizing the state and making the simulation nonphysical. The severity of denormalization can be determined by summing the probability amplitudes of all states up to the cutoff dimension. This quantity is referred to as a state trace. A fully normalized state has a state trace of 1 and low traces imply denormalized states and nonphysical simulation. Reducing state drift and maintaining state trace normalization is critical to successful simulation and training of hybrid networks.

2. State Trace Normalization Techniques

As mentioned in the previous section, a normalized trace is essential to a realistic simulation of CVQNN. During training the network can easily become denormalized so three methods to maintain normalization are used. A small network of three qumodes with classical layers on either side for dimension matching will be used to verify the

normalization methods. The maximum amplitude a_{max} was found by randomly initializing the amplitude parameters to the domain $[0, a_{max}]$ and the phase parameters to $[0, 2\pi]$ and then measuring the trace. The trace was measured with random weights in this domain until either the trace fell below a threshold or the network maintained normalization for 100 sets of random weights. If the trace fell below the threshold, a_{max} would be decremented by 0.01 and the process would repeat. In this way, the maximum amplitude that still maintains normalization can be found. This a_{max} is used to scale the inputs into the encoding layer and is the upper bound on the amplitude parameter uniform initialization. The top figure in Fig. 6a shows the trace if a_{max} is scaled by a constant. The networks naturally learn to normalize as they train, however, networks with scaled amplitudes saw a low initial trace. The middle figure in Fig. 6a then shows the benefit of the quantum preparation layer which scales the inputs to the encoding layer to fit in the domain for the amplitude, $[0, a_{max}]$ and phase parameters, $[0, 2\pi]$. Finally, the bottom figure in Fig. 6a shows the impact of regularization on the trace normalization. Regularization adds a term to the loss function that is proportional to the magnitude of amplitude parameters. High regularization maintains normalization but lowers performance.

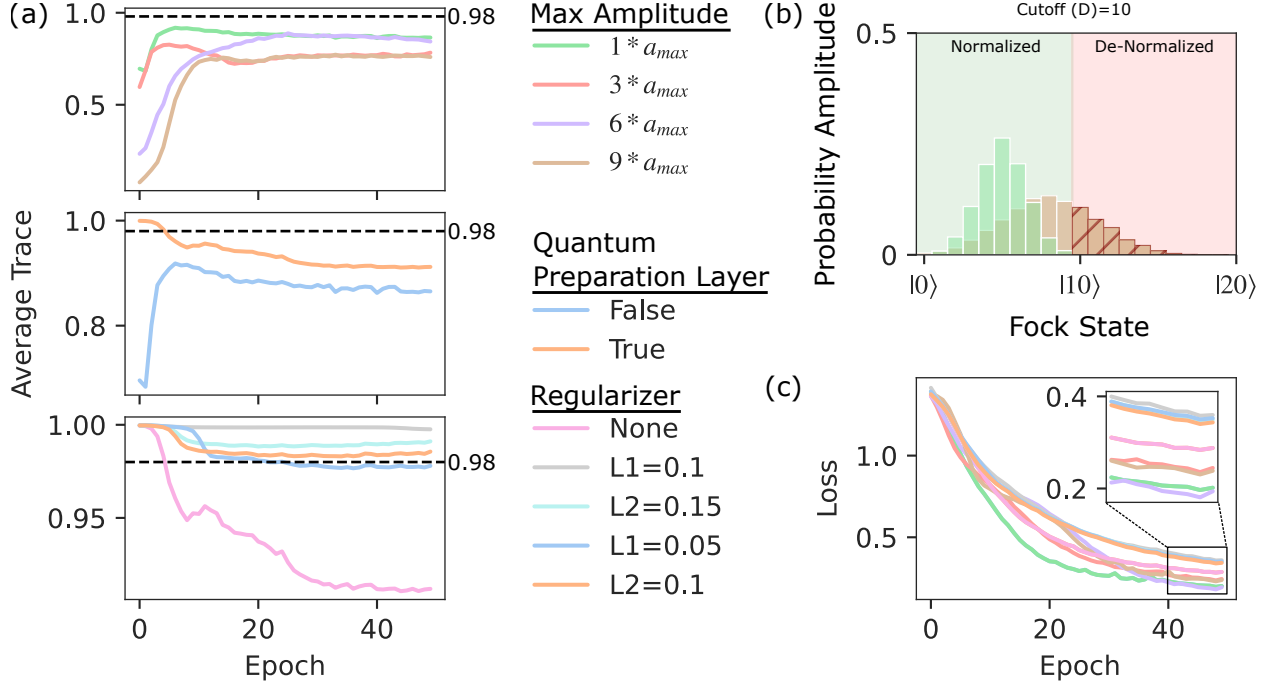


FIG. 6: (a) Plots showing the Fock state trace of networks as different normalization techniques are applied. (b) Demonstration of the Poisson distributions of a normalized and denormalized qumode. (c) The loss of the networks seen in (a) are plotted. Networks with good normalization or low regularization perform the best.

3. Parameter Shift Rule

Gradients are calculated using the parameter shift rule [23] which can be seen in (A1).

$$\nabla f(\theta) = c[f(\theta + s) - f(\theta - s)] \quad (\text{A1})$$

Where f is the quantum function of interest, c is a scaling constant, and s is shift constant. Determining s and c is dependent on the specific gate of interest [44, 45]. As an example, an x quadrature squeeze gate operation in the Heisenberg picture is defined by (A2)

$$\mathcal{M}(r) = S^\dagger \hat{x} S = e^{-r} \hat{x} \quad (\text{A2})$$

Where \hat{x} is an operator that return the x quadrature and r is the squeezing amplitude. Assuming an input $|y\rangle$ is operated on by $\mathcal{M}(r)$, the gradient would then be given by (A3) [30].

$$\nabla \langle y | \mathcal{M}(r) | y \rangle = \frac{1}{2\sinh(s)} [\langle y | \mathcal{M}(r+s) | y \rangle - \langle y | \mathcal{M}(r-s) | y \rangle] \quad (\text{A3})$$

Where s an arbitrary non-zero shift.

4. Hybrid Network Operation

Starting with the forward pass and an input vector \vec{x} the operation of the input layer.

$$\vec{y} = f(W^{(i)}\vec{x} + \vec{b}^{(i)})$$

The \vec{y} is then encoded into the quantum state using an encoding layer. An example for a single qumode encoded state $|\psi_0\rangle$ we have:

$$|\psi_0\rangle = \mathcal{D}(y_1, y_2) \mathcal{S}(y_3, y_4) \Phi(y_5) |0\rangle$$

$$|\psi_1\rangle = \dots$$

Then applying the CV neural network layer $\mathcal{L}^{(h)}$:

$$\mathcal{L}^{(h)} = \Phi(\kappa) \circ \mathcal{D}(\alpha) \circ \mathcal{U}_2(\vec{\theta}_2, \vec{\phi}_2) \circ \mathcal{S}(s) \circ \mathcal{U}_1(\vec{\theta}_1, \vec{\theta}_2)$$

This operation has single qumode operations $(\Phi, \mathcal{D}, \mathcal{S})$ which act individually on each qumode, and multiqumode operations $(\mathcal{U}_1, \mathcal{U}_2)$ which act on all qumodes together. The expectation value of state measurement in the position basis is given by the following:

$$\langle \hat{x}_0 \rangle = \langle \psi_0 | \mathcal{L}^{(h)} \hat{x} \mathcal{L} | \psi_0 \rangle$$

This gives an output vector \vec{z} equal in size to the number of qumodes.

$$\vec{z} = (\langle \hat{x}_0 \rangle, \dots, \langle \hat{x}_N \rangle)$$

This is inputted into the final output layer.

$$\vec{o} = \text{Softmax}(\hat{W}^{(o)}\vec{z} + \vec{b}^{(o)})$$

Finally, the error for each sample and the total loss for each batch is calculated.

$$E = \sum_{i=1}^4 p_i \log(o_i)$$

$$L = \frac{1}{N} \sum_{j=1}^N \sum_{i=1}^4 p_{ji} \log(o_{ji})$$

The we can calculate the partial derivative of the loss function with respect to each weight in the network.

$$\frac{\partial L}{\partial w_{00}^{(i)}} = \frac{\partial y_0}{\partial w_{00}} \frac{\partial \vec{z}}{\partial y_0} \frac{\partial \vec{o}}{\partial \vec{z}} \frac{\partial L}{\partial \vec{o}}$$

Finally, using these partial derivatives, we update the weights for one batch using gradient descent.

$$W_{i+1} = W_i - \eta \nabla_{W_i} L$$

This forward and backward pass is repeated for each batch in the training dataset which represents one epoch. The networks were then trained for a total of 200 epochs.

5. Raw Loss Curves

Here we saw the raw training curves of all the networks presented in this study. In the hybrid case, Fig. 7, the accuracy increases for larger networks and larger cutoff dimensions. For the classical networks, Fig. 8, we see a much broader distribution of training, a solid line at random prediction, but still the same correlation between network size and performance.

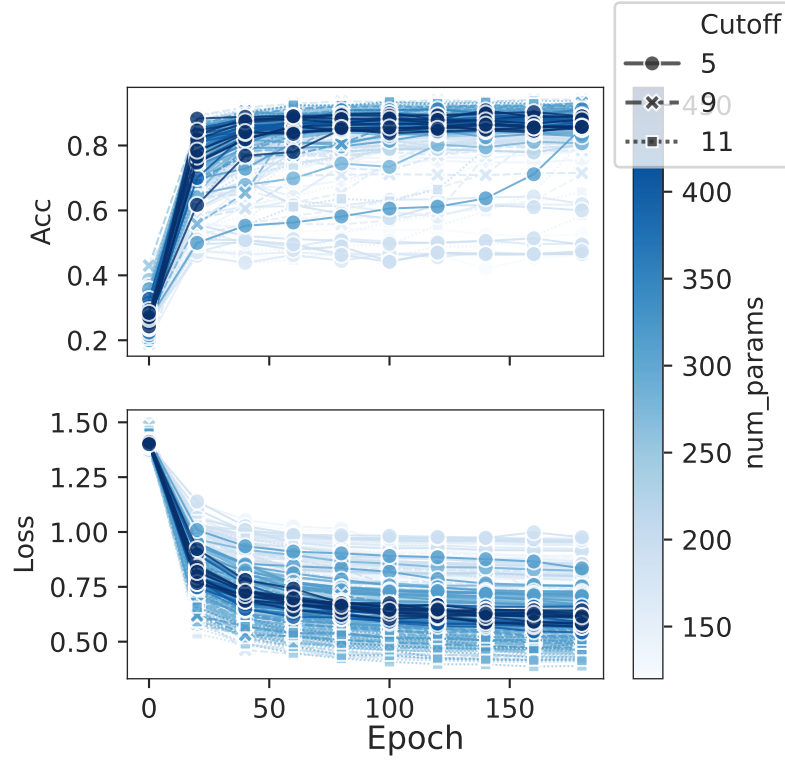


FIG. 7: Raw hybrid network training data.

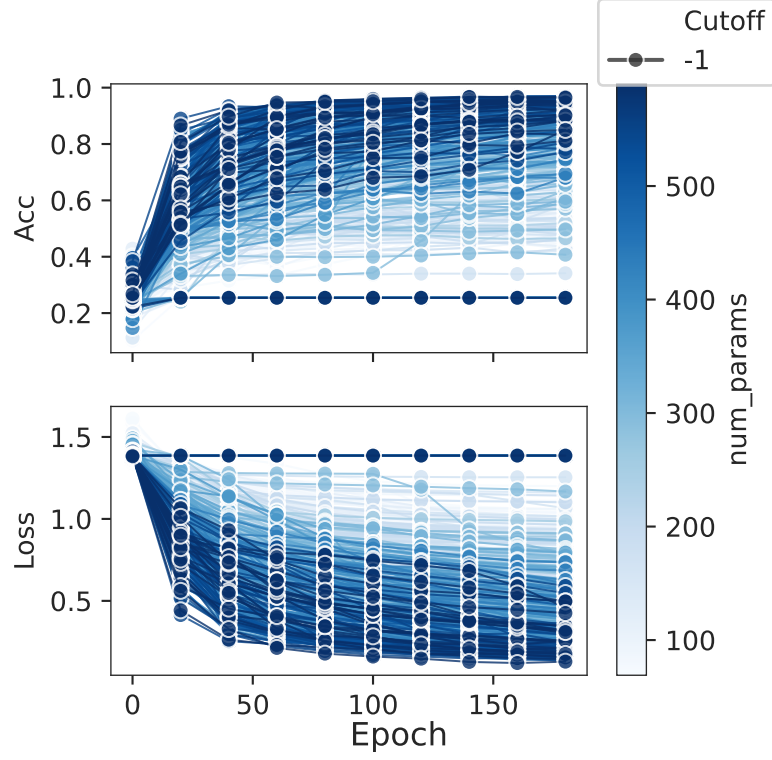
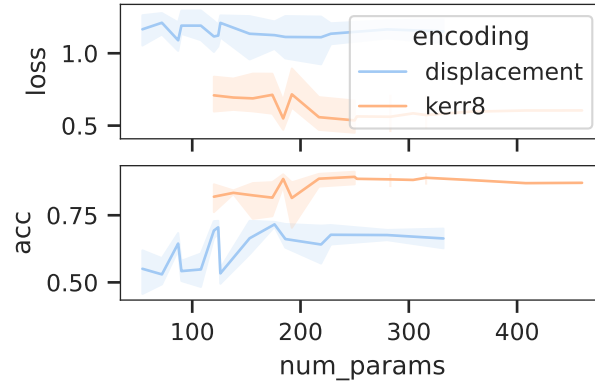


FIG. 8: Raw classical network training data.

6. Encoding Comparison

The encoding scheme used in this work is complex and computationally difficult to simulate. If instead we only use a displacement gate for encoding, we can see a significant drop in network performance.



7. PCA and Linear Fitting

Here is a projection of the 8 dimensional dataset explored projected onto a two dimensional space using principle component analysis. In this low dimensional space, we then fit the data using a support vector machine (linear model) [22]. The data and classification boundaries in this two dimensional space can be seen in Fig. 9.

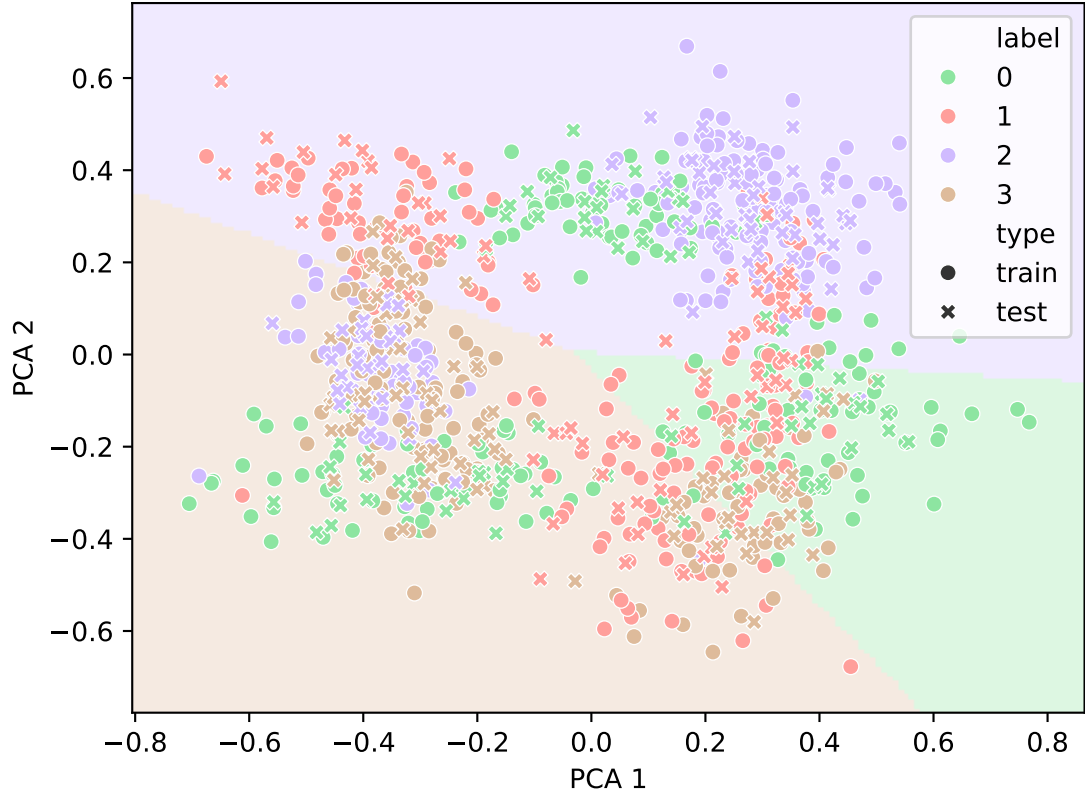


FIG. 9: State vector machine classification boundaries on dimensionally reduced dataset. This model achieved 0.41 training accuracy and 0.39 testing accuracy.

With the same two dimensional dataset we can also fit a Kmeans clustering model seen in Fig. 10. In both the state vector machine and Kmeans case, the linear model struggles to classify the data in this low dimensional space.

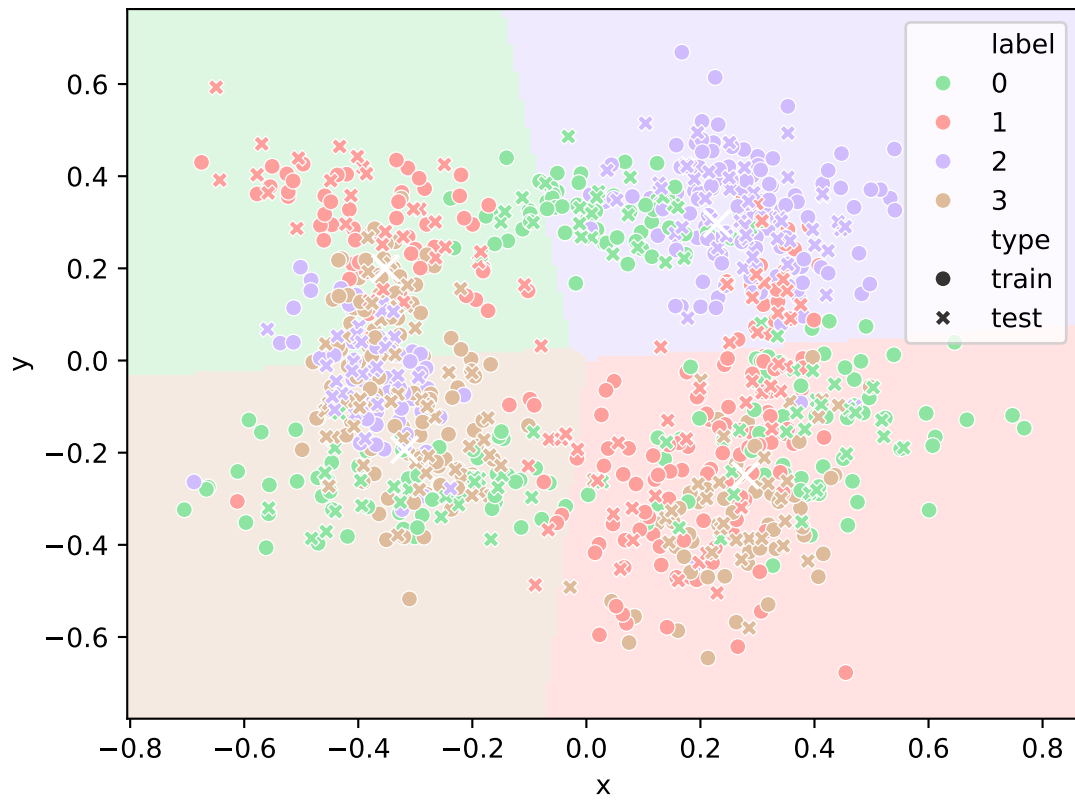


FIG. 10: Kmeans clustering on dimensionally reduced dataset. This model achieved 0.42 training accuracy and 0.36 testing accuracy.